A Detailed Picture of Haiti's Seismicity Given by Deep Learning and Template Matching

Miguel Neves*[1,2], Quentin Bletery[1], Françoise Courboulex[1], David Ambrois[1],
Jérôme Chèze[1], Tony Monfret[1,3], Steeve Symithe[4], Sylvert Paul[1,4], Louis De Barros[1],
Bryan Raimbault[5,6], and Éric Calais[5]

Abstract

Haiti regularly experiences destructive earthquakes, but seismic monitoring in the region has historically been limited. Recent deployments of citizen-hosted RaspberryShake seismometers and temporary seismic deployment following the 2021 M_w 7.2 earthquake provide new data to study the region's seismotectonics. However, high noise levels at many stations, in particular the RaspberryShake ones, limit detection, hence the fault imaging capability of these instruments. This study explores the use of a Deep Learning denoising algorithm, DeepDenoiser, to improve their seismic signal and earthquake detection capabilities. We find that DeepDenoiser raises the average signal-to-noise ratio of seismic signals by 4.7 dB and increases earthquake detections, but also raises false detections when using short-term average/long-term average and deep learning detection methods. Template matching, however, when combined with DeepDenoiser, yields more true detections and fewer false detections than traditional band-pass-filtered waveforms. This suggests that DeepDenoiser is better suited for retrospective studies than for real-time applications. Using DeepDenoiser and template matching, we compile a 2 yr, high-resolution earthquake catalog for Haiti containing about three times the number of events of the original catalog. The improved catalog furthers our understanding of the 2021 M_w 7.2 earthquake sequence, highlighting particularly clearly the segmented nature of the aftershock distribution with a generally northeast-dipping cluster in the east that coincides with the hypocenter and first reverse phase of the rupture, and a series of aftershocks farther west that coincide with the mostly strike-slip phase of the rupture. The improved catalog also reveals potentially fluid-induced offshore seismic swarms in the Jérémie basin and active seismicity below Lake Enriquillo in the Dominican Republic. This catalog advances our understanding of the region's seismicity and provides further opportunities to study the larger regional tectonic context.

Cite this article as Neves, M., Q. Bletery, F. Courboulex, D. Ambrois, J. Chèze, T. Monfret, S. Symithe, S. Paul, L. D. Barros, B. Raimbault, *et al.* (2026). A Detailed Picture of Haiti's Seismicity Given by Deep Learning and Template Matching, *Seismol. Res. Lett.* **XX**, 1–15, doi: 10.1785/0220250412.

Supplemental Material

Introduction

Our understanding of fault systems and earthquakes relies on regional efforts to monitor seismic activity and build comprehensive earthquake catalogs. Creating these catalogs involves multiple step workflows, including seismic data recording, earthquake detection, phase picking, association, location, and magnitude estimation, whose accuracy is strongly influenced by the signal-to-noise ratio (SNR) of seismic recordings. Historically, earthquake monitoring relied on manual phase picking, but this is impractical with growing data volumes. Energy-based automatic detection methods, such as the short-term-average to long-term-average (STA/LTA) trigger (Allen, 1978), have since been developed but provide coarser

---

1. Observatoire de la Côte d'Azur, Université Côte d'Azur, IRD, CNRS, Geoazur, Sophia Antipolis, Valbonne, France, https://orcid.org/0000-0002-8581-8551 (MN); https://orcid.org/0000-0002-9796-5487 (QB); https://orcid.org/0000-0002-4467-9102 (FC); https://orcid.org/0000-0003-1155-5645 (DA); https://orcid.org/0000-0002-7644-3989 (JC); https://orcid.org/0000-0002-4521-0357 (TM); https://orcid.org/0000-0003-4132-7635 (SP); https://orcid.org/0000-0002-5541-9162 (LDB); 2. Now at Department of Earth Science, University of Bergen, Bergen, Norway; 3. Barcelona Center for Subsurface Imaging, Institut de Ciències del Mar (ICM), CSIC, Barcelona, Spain; 4. URGéo, Faculté des Sciences, Université d'État d'Haïti, Port-au-Prince, Haïti, https://orcid.org/0000-0003-1133-202X (SS); 5. Département de Géosciences, École normale supérieure, Université PSL, Paris, France, https://orcid.org/0000-0001-9561-6171 (BR); https://orcid.org/0000-0002-5935-8117 (EC); 6. University of Grenoble Alpes, University of Savoie Mont Blanc, CNRS, IRD, University of Gustave Eiffel, ISTerre, Grenoble, France

*Corresponding author: migueljgneves@gmail.com

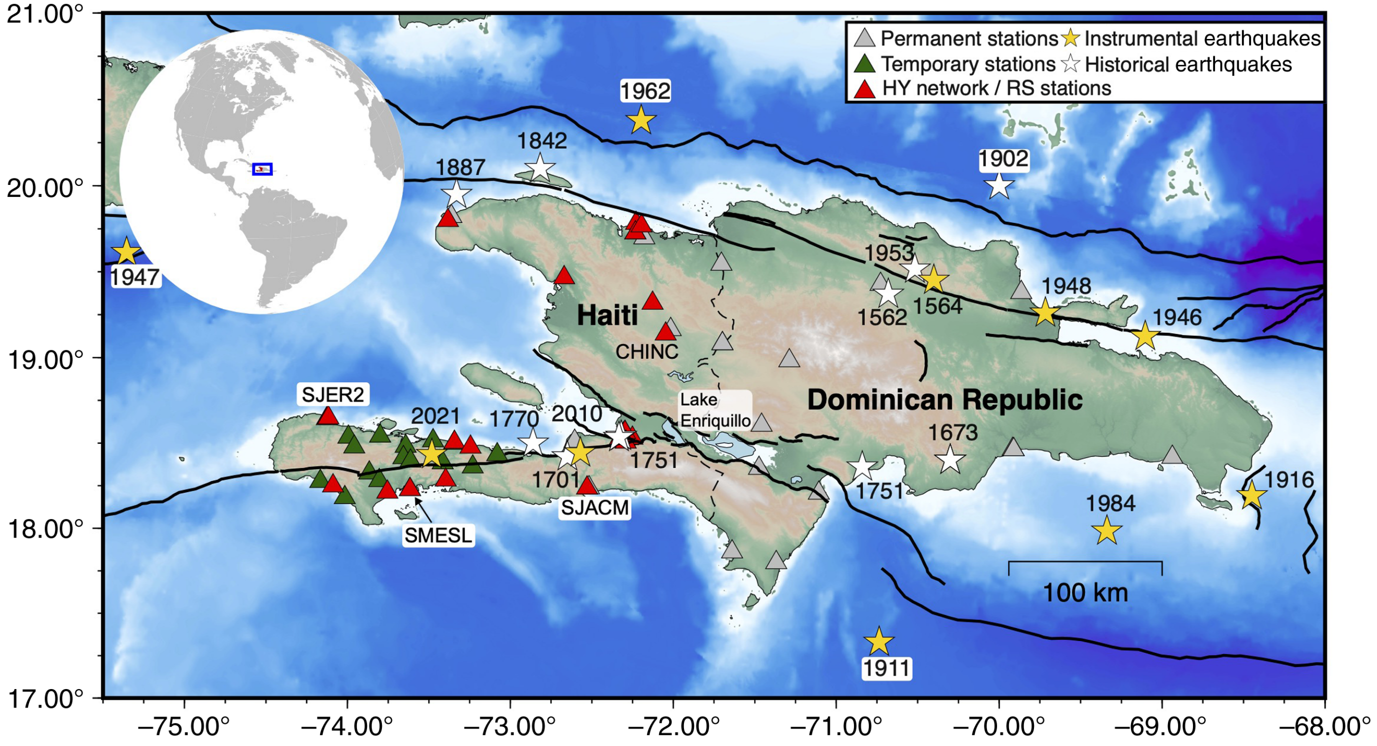

Figure 1. Map of Hispaniola showing seismic stations used in our study. Seismic stations are denoted by triangles: the HY network in red, temporary deployments in green, and permanent stations with publicly available data in gray. The stars mark major historical (white) and instrumentally recorded (yellow) events. The black lines indicate active fault traces by Styron *et al.* (2020). The color version of this figure is available only in the electronic edition.

results, often generating false detections due to noise from nontectonic impulsive signals, requiring manual review. As a result, earthquake catalogs remain incomplete (Kagan, 2004; Peng *et al.*, 2006), particularly during time intervals of high background noise such as after a large earthquake.

Deep learning methods offer new opportunities to address this limitation. Phase pickers such as ConvNet (Ross *et al.*, 2018), PhaseNet (Zhu and Beroza, 2019), and EQTransformer (Mousavi *et al.*, 2020), and emerging end-to-end systems (van den Ende and Ampuero, 2020; Münchmeyer *et al.*, 2021; Licciardi *et al.*, 2022; Hourcade *et al.*, 2025) have shown promise, but their performance is ultimately constrained by the noise level in the waveforms. Recently, deep learning denoisers have been introduced to remove overlapping noise and enhance seismic signals (Zhu *et al.*, 2019; Dahmen *et al.*, 2022). These tools can outperform traditional filtering because they separate noise from signal even when their frequency bands overlap. However, few studies have quantitatively evaluated their performance on continuous, real-world seismic data (Dahmen *et al.*, 2022; Yang *et al.*, 2022).

In this study, we explore the potential gain in using recently developed deep learning tools for earthquake monitoring in Haiti. The island of Hispaniola, including Haiti and the Dominican Republic, is situated along a transpressional section of the Caribbean–north America plate boundary (Calais *et al.*, 2016). This seismotectonic environment has resulted in numerous severe earthquakes throughout history (e.g., Bakun *et al.*, 2012). More recently, the 2010 M_w 7.0 Haiti earthquake, which caused over 200,000 fatalities and economic losses close to 100% of the country's gross domestic product (Calais *et al.*, 2010) and the 2021 M_w 7.2 Nippes earthquake (Calais *et al.*, 2022) highlighted the need for reliable earthquake monitoring. Despite considerable natural, economical, and political constraints (Corbet *et al.*, 2024), Haiti now maintains an operational real-time earthquake monitoring system (Calais *et al.*, 2020, 2022). The network relies primarily on citizens' hosted, low-cost RS4D RaspberryShake (RS) sensors (HY network; Fig. 1), supplemented by temporary and permanent stations across the region with publicly open data streams (Paul *et al.*, 2023). The data are streamed in real time to a monitoring platform, coined Ayiti-seismes, which has operated continuously since August 2019 and uses a STA/LTA algorithm detector followed by manual review. The Ayiti-seismes system has enabled a significantly improved monitoring of the region with an estimated magnitude of completeness (M_c) of 2.5. The improved monitoring provided critical data to understand the 2021 M_w 7.2 Nippes earthquake (Calais *et al.*, 2022), revealing a multiple segment rupture. However, as reported by Paul *et al.* (2023), RS stations have higher noise levels than broadband stations because they are installed in urban settings,

TABLE 1
Signal-to-Noise Ratio (SNR) and Signal Distortion Ratio (SDR) for the Different Pretrained and Retrained DeepDenoiser Models

	Pretrained			**Retrained DeepDenoiser**		
Metrics	**Raw Waveforms**	**DeepDenoiser**	**UrbanDenoiser**	**Entire Network**	**Last Layer**	**First Layer**
SNR	15	34.42	17.66	35.44	32.51	34.86
SDR	–	6.74	6.48	5.36	4.59	5.83

Only results for the models with the lowest validation loss for each hyperparameter configuration are shown.

inside volunteers' homes, and without prior evaluation of background noise, reducing detection performance.

Here, we test whether applying a deep-learning denoiser can mitigate these noise conditions and how it impacts commonly used automatic earthquake detectors. Using the HY network together with a temporary deployment of 12 broadband stations installed after the 2021 M_w 7.2 Nippes earthquake (Z2; Douilly *et al.*, 2022), we also construct a two-year high-resolution catalog (January 2021–December 2022) as a proof of concept for the improvements in detection that denoising can enable, revealing previously unidentified clusters of seismic activity.

Denoising

To enhance the quality of seismic waveforms recorded in Haiti, we apply the DeepDenoiser deep learning algorithm (Zhu *et al.*, 2019). DeepDenoiser is a convolutional neural network trained to separate earthquake signals from noise in the frequency domain. It takes spectrograms of noisy signals as input and outputs a signal and a noise mask, which are applied to the input signal to obtain the denoised signal. The original DeepDenoiser model was trained on an extensive dataset of earthquake and noise signals recorded in northern California (Zhu *et al.*, 2019).

We test different DeepDenoiser models before applying them to continuous Haiti data: (1) the original DeepDenoiser model (Zhu *et al.*, 2019), (2) UrbanDenoiser, a version retrained on the Long Beach (California, United States) focusing on urban environments (Yang *et al.*, 2022), and (3) models retrained on Haiti data. For retraining, we use 4957 30-s-long earthquake waveforms with SNR above 10 dB from the Ayiti-seismes catalog, and 5976 noise waveforms listed as "Not earthquakes" after applying the PhaseNet picker (Zhu and Beroza, 2019) to ensure no seismic phase is present. The dataset is split into training, validation and testing datasets in a 80%/10%/10% ratio. We retrain the model starting with the original DeepDenoiser weights, testing different retraining approaches (entire network, first layer, and last layer), learning rates (10^{-2} to 10^{-6}), batch sizes (50, 100, 200, and 500), and dropout rates (0, 0.01, 0.05, 0.1, and 0.25). We used cross-entropy loss and stopped training once there was no validation loss improvement for 10 epochs, saving the epoch with best validation loss. For each epoch, each signal waveform is merged with all noise waveforms randomly scaling its amplitude to create multiple "noisy" signals (Zhu *et al.*, 2019). To assess performance, we calculate the SNR and signal distortion ratio (SDR) of the test dataset waveforms (Zhu *et al.*, 2019; Yang *et al.*, 2022) using:

$$\mathrm{SNR} = 10 \log_{10} \frac{\sigma_{\mathrm{signal}}}{\sigma_{\mathrm{noise}}}, \tag{1}$$

and

$$\mathrm{SDR} = 10 \log_{10} \frac{\| W_{\mathrm{GT}} \|}{\| W - W_{\mathrm{GT}} \|}, \tag{2}$$

in which W is the denoised waveform, W_{GT} the ground-truth waveform, σ_{signal} the standard deviation of the signal, and σ_{noise} the standard deviation of the noise. High SDR indicates lower distortion, reflecting better separation of the signal of interest from noise.

Results from our tests of transfer learning and fine-tuning DeepDenoiser models on the Haiti test dataset are shown in Table 1. For each combination of dropout rate, batch size, and learning rate, we present the model with the lowest validation loss. Based on SNR metrics, retraining the entire network or just the last layer shows a slight improvement over the original DeepDenoiser model. However, when considering the average SDR estimates, the retrained models perform worse than the original model. This suggests that retrained models not only remove more noise before the first-phase arrival, but also misidentify more signal as noise, leading to higher waveform distortion. Notably, the UrbanDenoiser model, trained on urban data with large anthropogenic noise, performs worse than the original DeepDenoiser model and any of the retrained models.

Based on these results, we choose to use the original DeepDenoiser model for denoising in the rest of this study (Fig. 2) as it presents the best balance of SNR and SDR (Table 1).

We apply the original DeepDenoiser model to all *P*-phase picks in the Ayiti-seismes catalog, including those with SNR $<$ 10 dB, and compute SNRs for denoised and non-denoised waveforms (Fig. 3). The average SNR increases by 4.7 dB across the full dataset and by 4.3 dB for the RS stations, indicating that DeepDenoiser improves signal quality similarly

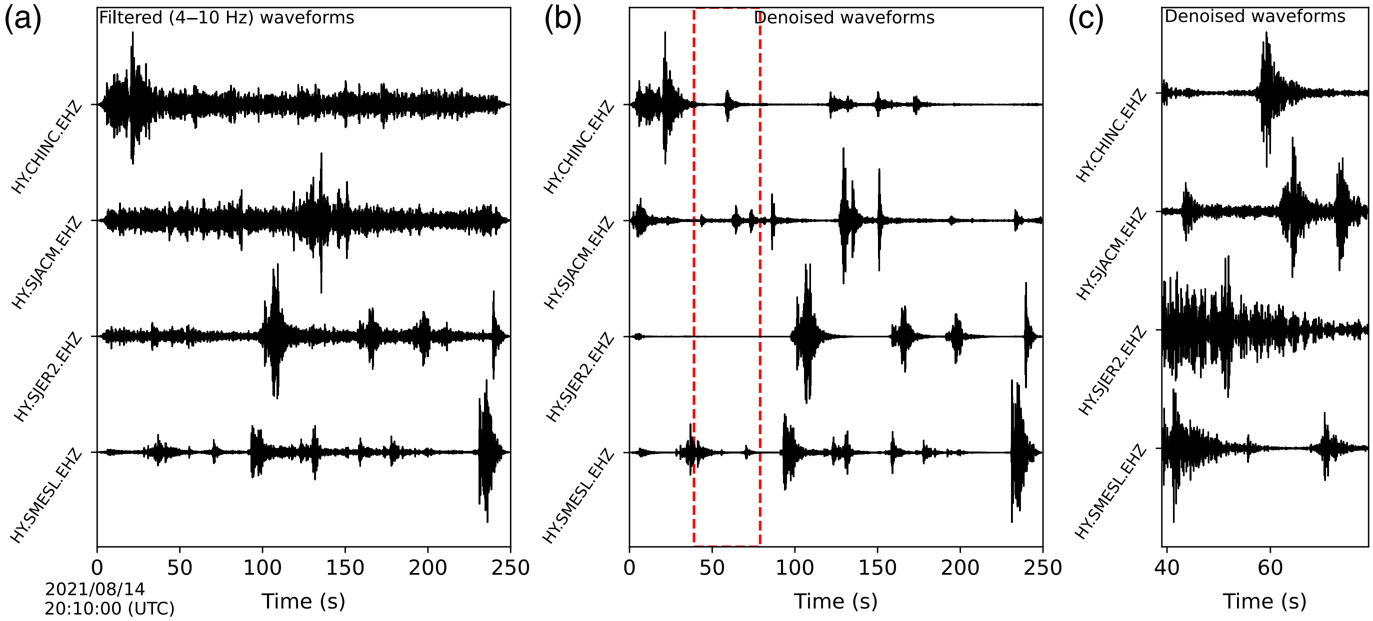

Figure 2. Examples of waveforms recorded on RS stations in Haiti. (a) Band-pass filtered (4–10 Hz). (b) Denoised using the original DeepDenoiser model. (c) Zoomed view of the highlighted interval in (b), illustrating the artifacts discussed in the text on stations CHINC and SJACM. Station locations are shown in Figure 1. The color version of this figure is available only in the electronic edition.

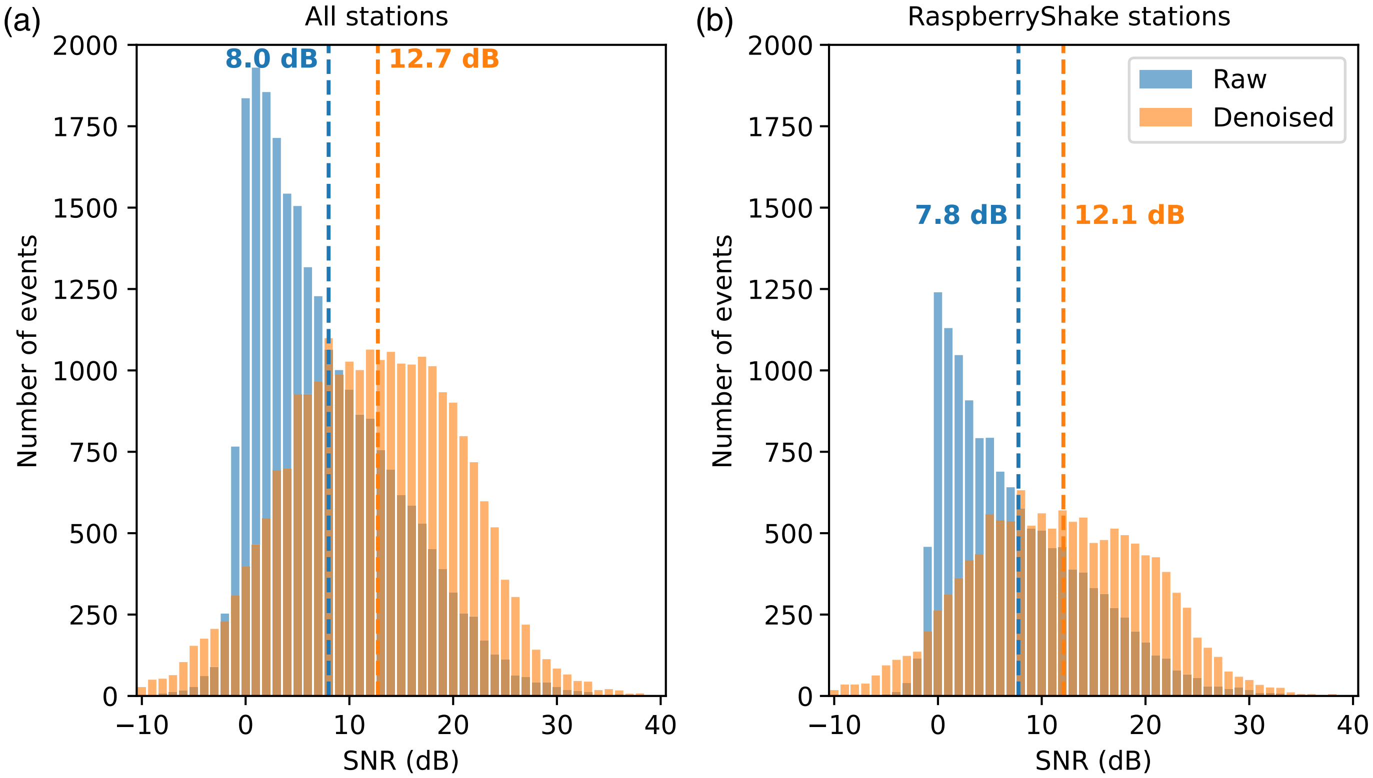

Figure 3. Signal-to-noise ratio (SNR) distributions of cataloged phase picks using raw (blue) and denoised waveforms (orange). Panel (a) includes all stations on Hispaniola, and panel (b) only the HY network. Negative SNRs reflect imprecise phase picks (see Fig. S2). The dashed lines indicate the mean of each distribution. The color version of this figure is available only in the electronic edition.

for the entire catalog and for the RS instruments, even though waveforms from RS instruments were absent from the training set.

Detection

To assess the impact of denoising on earthquake detection, we apply three detection methods: STA/LTA detector (Allen, 1978), PhaseNet deep learning picker (Zhu and Beroza, 2019), and template matching detection (Gibbons and Ringdal, 2006).

We perform detection on all the stations available in the island (Fig. 1, Table S1, available in the supplemental material to this article). To ensure a fair comparison, we established consistent source–station distances and corresponding detection time windows for analysis. We determined a distance threshold by examining the distribution of source–station distances for the earthquakes in our catalog (Fig. S1a). This distribution exhibited a clear bimodal pattern, with a noticeable decrease in the number of phase picks around 120 km, and a dominant first mode containing a higher number of phase picks. This bimodal shape reflects the island's geography, as most stations are concentrated on its western side. Therefore, we selected 120 km as the distance threshold, focusing our analysis on the dominant mode and local distances, similar to those used to train the DeepDenoiser and PhaseNet models (Zhu and Beroza, 2019; Zhu *et al.*, 2019). This distance threshold corresponds to an approximate *S*–*P* time difference of 15 s (Fig. S1b).

We apply STA/LTA and PhaseNet to single-station waveforms separately, whereas we apply template matching to the entire network waveforms. Therefore, we must perform an association of the STA/LTA and PhaseNet phase picks, which we do using the Rapid Earthquake Association and Location method (REAL) (Zhang *et al.*, 2019).

To compare the different detection methods, we apply them to band-pass filtered, denoised, and denoised-and-band-pass-filtered waveforms. We then compare the number of detections and their quality by visual inspection. For PhaseNet, we also compare raw waveform detections. We apply DeepDenoiser to continuous data, using the Seisbench package tools (Woollam *et al.*, 2022), processing 30 s windows of data with an overlap of 15 s (taking the average of overlapping segments).

STA/LTA

The STA/LTA method (Allen, 1982) is a detection technique widely used in real-time monitoring systems (e.g., Helmholtz-Centre Potsdam–GFZ German Research Centre for Geosciences and Gempa GmbH, 2008). It computes the ratio of a short-term window's average (STA) amplitude to a long-term window's average (LTA) amplitude. Once this STA/LTA ratio exceeds a predefined threshold, a detection is declared. We test STA/LTA using the parameters used in Ayiti-seismes (Paul *et al.*, 2023). We use ObsPy's recursive STA/LTA function (Beyreuther *et al.*, 2010) with a 1 s short window, a 30-s-long window, and a trigger threshold of 2.5. Detection of *P* phases is performed on the vertical components, and *S* phases on the average envelope of the horizontal components.

PhaseNet

PhaseNet is a deep learning model that identifies seismic phase arrivals (Zhu and Beroza, 2019). PhaseNet is widely used in deep learning earthquake detection workflows (e.g., Liu *et al.*, 2020; Tan *et al.*, 2021; Wickham-Piotrowski *et al.*, 2024). It analyzes three-component waveforms, evaluating the probability that a trace contains a *P* or *S* wave or noise. Similar to the original DeepDenoiser model, the original PhaseNet was trained on waveforms from the Northern California earthquake catalog. We use the Seisbench-implemented original PhaseNet model (Woollam *et al.*, 2022), applying it to 30 s windows of 100 Hz continuous data with 15 s steps. A *P*- or *S*-phase detection is declared if the respective probability exceeds 0.1.

Association

In the case of STA/LTA and PhaseNet, we associate detected picks using REAL (Zhang *et al.*, 2019). REAL is an associator that counts phase picks along theoretical travel-time windows, for which we use the velocity model inverted by Douilly *et al.* (2022). The grid-search parameters we use for the theoretical travel-time calculations are 1.2° with 0.05° steps for the horizontal distance and 40 km with 2 km steps for depth. We allow an earthquake detection every 10 s, limiting the maximum source–station distance to 120 km and requiring at least four *P*-phase picks and two *S*-phase picks for a detection.

Template matching

Template matching detects similar seismic events by cross-correlating waveforms of cataloged events with continuous waveforms (e.g., Gibbons and Ringdal, 2006; Neves *et al.*, 2022). We implement template matching using a network-based approach with the fast matched filter code of Beaucé *et al.* (2017), running on graphics processing units and using all available broadband components of each station.

We use events from Ayiti-seismes' catalog as templates, selecting events with at least four *P*-phase picks with source–station distances <120 km and SNR > 5. For these events, we use a time window from 1 s before the *P*-phase arrival to 16 s after, including also the *S*-phase arrival. We cross-correlate each template with continuous waveforms from the corresponding station, processing the continuous data in consecutive 1 hr windows using a one-sample sliding step. To improve the SNR of the cross-correlation function (CCF), we shift and stack the CCFs of the entire network and declare a detection if the stacked CCF is above 26 times the median absolute deviation.

Impact of denoising on earthquake detection

To assess the impact of denoising the waveforms recorded in Haiti considering the aforementioned detection methods, we

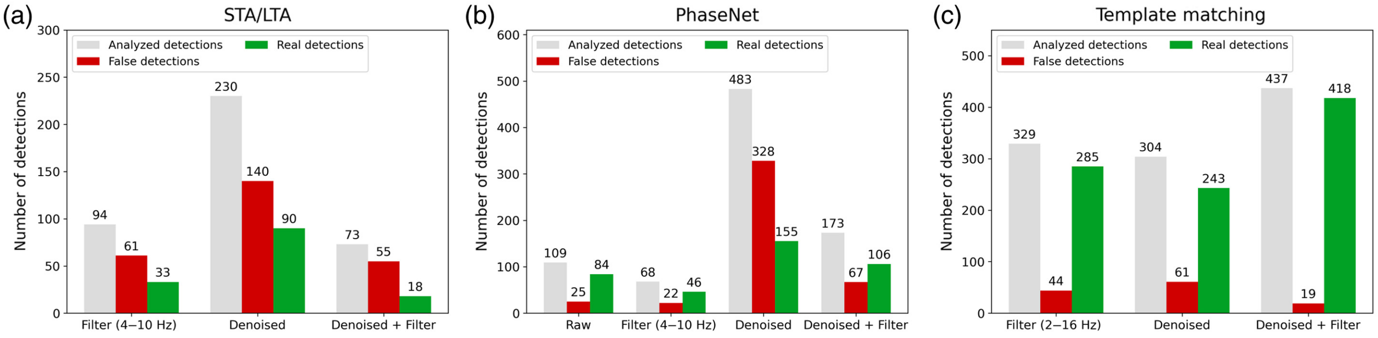

Figure 4. Comparison of detection tests using denoised and non-denoised waveforms. (a) Short-term average/long-term average (STA/LTA) detection on filtered, denoised, and denoised-and-filtered waveforms. (b) PhaseNet detection on raw, filtered, denoised, and denoised-and-filtered waveforms. (c) Template matching detection on filtered, denoised, and denoised-and-filtered waveforms. The gray bars represent total detections, green bars represent real detections, and red bars represent detections. The color version of this figure is available only in the electronic edition.

visually inspect the obtained catalogs during two time intervals: from 1 to 26 August, an interval that includes detections before the deployment of the temporary broadband network and the early aftershock period of the 2021 mainshock, and 6 and 7 November, the 2 days with the highest number of working stations in the dataset. Histograms summarizing the classification of detected events as real and false detections are shown in Figure 4. The detection methods were tested on band-passed filtered and denoised waveforms for all methods, and also on "raw" waveforms, that is, removing only the trend, for PhaseNet detections, since PhaseNet was trained on unfiltered waveforms.

Considering only the detection numbers, PhaseNet applied to denoised waveforms returns the highest number of detections. However, when inspecting these detections, we find that more than 60% of them correspond to the detection and association of impulsive artifacts resulting from the denoising process. A similar result is obtained using STA/LTA with denoised waveforms: a higher number of events is detected, but the majority corresponds to artifacts. For PhaseNet, the best ratio of real detections is observed when applying the detector with raw waveforms, even though it misses detections found only in denoised waveforms. In contrast, template matching performs best using denoised waveforms followed by a band-pass filter. This strategy returns fewer false detections and more real detections than applying template matching on only band-pass-filtered waveforms or only denoised waveforms. It further returns a higher number of real detections than any strategy using PhaseNet and STA/LTA, and almost 1.5 times more real detections than template matching with band-pass-filtered waveforms.

Combining Denoising and Template Matching to Compile a New Catalog

Considering the performances of the methods tested here (Fig. 4), we apply template matching detection to denoised and band-pass filtered (2–16 Hz) waveforms to build an enhanced earthquake catalog in Haiti. To do so, we use 2065 templates and search in all continuous waveforms available from January 2021 to December 2022. Magnitudes of the newly detected events were estimated using relative magnitude estimation (see Fig. S3). The detection process yields a catalog of 13,877 events, compared with 3,617 events in the Ayiti-séismes catalog. However, 1736 events listed in Ayiti-séismes are not detected by our workflow (Fig. S4). These include events that could not be detected or used as templates due to station outages, limited network coverage, and waveform clipping (including the M_w 7.2 mainshock). In particular, in the days immediately following the mainshock, fewer than four nearby stations were operating, which prevented many events in the area from meeting our minimum station requirement. This apparent discrepancy results from our detection thresholds requiring events to be recorded at a minimum of four stations within 120 km. When the same criteria are applied to the Ayiti-séismes catalog, only 31 events are not detected by our workflow.

We locate the new events using HypoDD (Waldhauser and Ellsworth, 2000), which determines relative earthquake locations by minimizing observed and theoretical travel-time difference residuals for pairs of earthquakes recorded at the same station, reducing errors from velocity-model mismatches. We use cross-correlation-derived differential travel times, computing the travel-time differences using denoised waveforms band-pass filtered between 2 and 16 Hz. We cross-correlate each event with all events in a 5 km radius or the 10 closest events—whichever is larger—using −0.2 to 1.3 s windows around *P*- and *S*-phase arrivals. We consider all measurements with a cross-correlation coefficient (CCC) > 0.6, and only keep pairs with at least five measurements and an average CCC > 0.7, ensuring at least three stations in common. To avoid measurements from spurious high CCC values, we recalculate CCCs using a 2 s window waveform and discard any travel-time measurement for which the maximum CCC differs by more than one sample. We use the Douilly *et al.* (2022) velocity model to locate the events.

(a) New catalog - 11,752 earthquakes

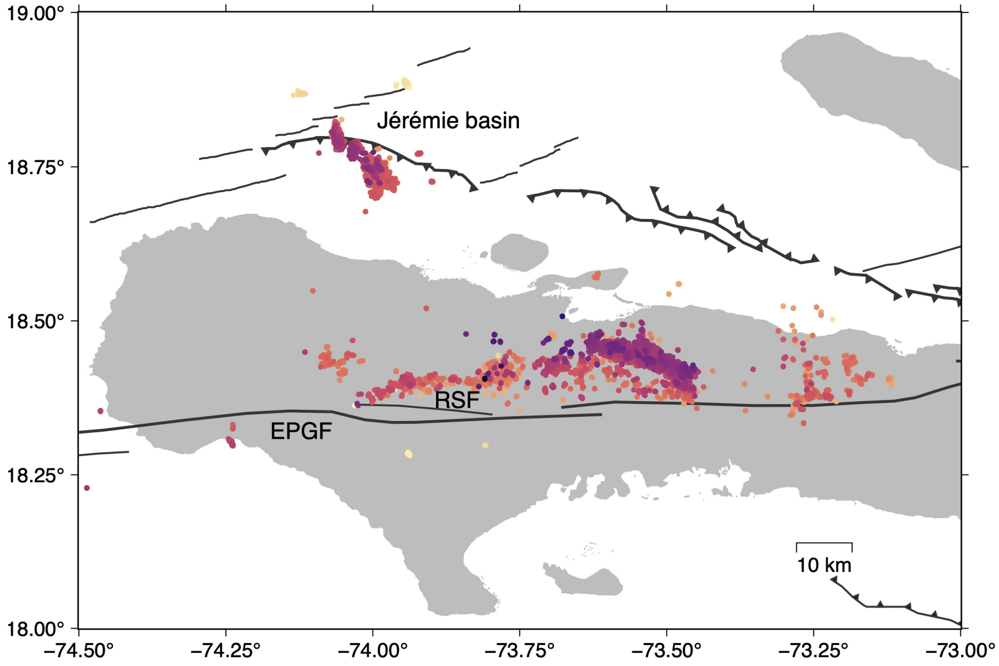

(b) Ayiti-seismes - 3,617 earthquakes

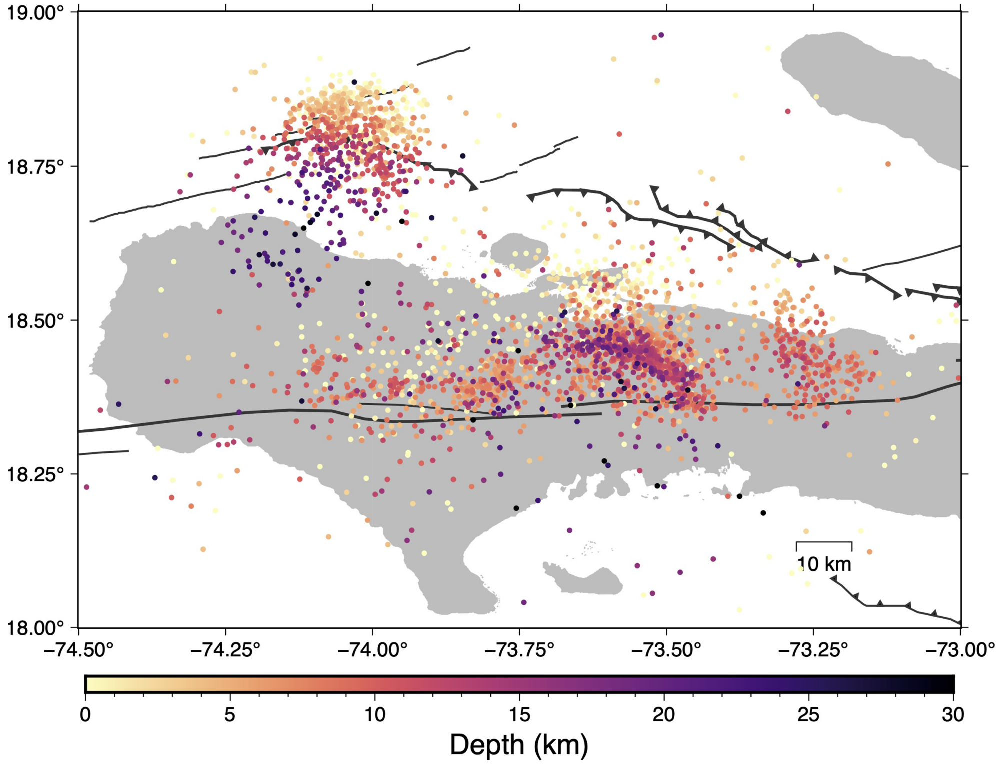

Figure 5. Catalog comparison with Ayiti-seismes earthquake catalog (1 January 2021–31 December 2022). (a) New catalog for the same time period. (b) Catalog from the Ayiti-seismes platform. The color denotes depth. EPGF, Enriquillo-Plantain Garden fault, RSF, Ravine du Sud fault. The color version of this figure is available only in the electronic edition.

The relocation results in a final catalog of 11,752 events (Figs. 5–7, Fig. S5). The majority of nonrelocated events corresponds to the largest magnitude events, a consequence of deteriorated CCC measurements between events with large-magnitude differences (Bachura and Fischer, 2019). In addition, poor waveform quality following the 2021 mainshock, with fewer continuously working stations and increased data gaps at this time, results in a significant number of nonrelocated events (325) in the 10 days after the mainshock.

To confirm the positive impact of denoising on the final catalog, we apply the same template matching detection and relocation procedure to only band-pass-filtered waveforms (2–16 Hz) for August–November 2021. This test results in a catalog of 6774 events using the filtered waveforms compared with 7393 events when using denoised waveforms. Furthermore, using filtered waveforms, the relocated events pair on average with 59 events and have an average relative location uncertainty of 20 m, whereas using the denoised waveforms, each event pairs on average with 100 events and has an average uncertainty of 14 m. Template matching is the biggest net contributor to the improved catalog, but denoising further reveals new events and improves locations by providing more differential travel-time information data.

The final catalog presents 11,752 precisely located events, which is about three times the number of events in the Ayiti-seismes catalog for the same

Jérémie basin and the Enriquillo lake in the Dominican Republic. We note that our catalog is biased toward sources similar to those already present in the Ayiti-seismes catalog due to the characteristics of template matching and double-difference relocation, limiting improvements for background or isolated seismicity.

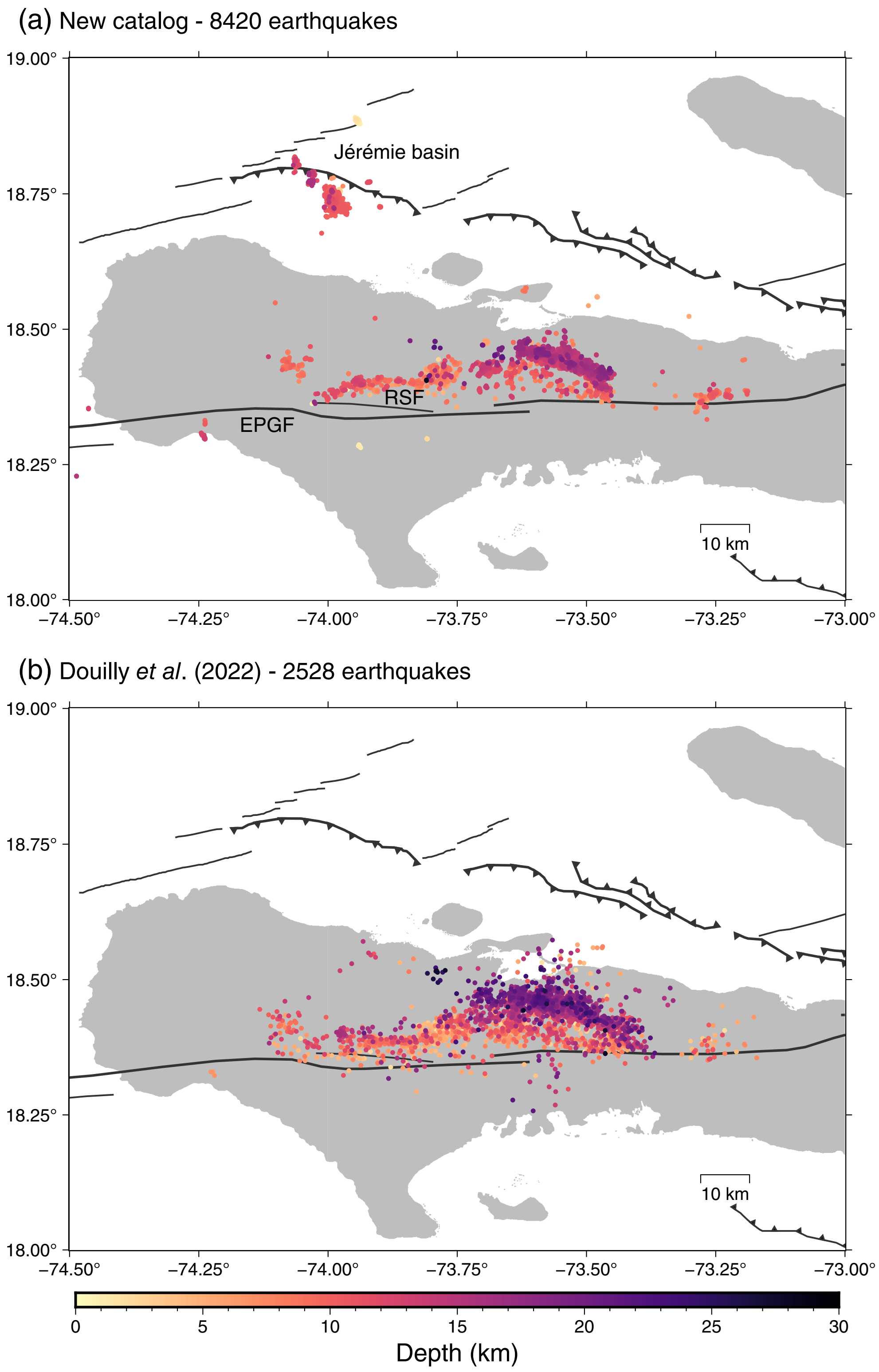

Figure 6. Comparison with Douilly *et al.* (2022) earthquake catalog (20 August 2021–30 December 2021). (a) New catalog for the same time period. (b) Douilly *et al.* (2022) catalogue. Color and fault abbreviations as in Figure 5. The color version of this figure is available only in the electronic edition.

Discussion

On the use of denoising for earthquake monitoring in Haiti

Our findings indicate that DeepDenoiser is better suited for detailed seismicity analyses than for automatic detection workflows. Our comparative tests using STA/LTA (Fig. 4a), the method used by Ayiti-seismes and commonly adopted by earthquake monitoring agencies (e.g., González, 2017; Duverger *et al.*, 2021), reveal that denoising significantly increases false alerts, increasing analysts' workload. In addition, employing DeepDenoiser followed by a band-pass filter yields fewer detections compared with traditional band-pass filtering. This discrepancy arises from variations in picking times that complicate the association process. DeepDenoiser zeros the amplitude of segments deemed pure noise, leading to subtle fluctuations being misinterpreted as phase onsets. Consequently, *P* phases are often picked earlier than manual picks or from the standard STA/LTA method. Combining DeepDenoiser with PhaseNet increases both false and real detections (Fig. 4b). However, PhaseNet was not retrained on local nor denoised waveforms; it is therefore possible that better results can be achieved in any of these

time interval (3617). Most of the newly detected events are located in the 2021 Nippes mainshock area, but the new catalog also reveals clear clusters of seismicity in other regions like the

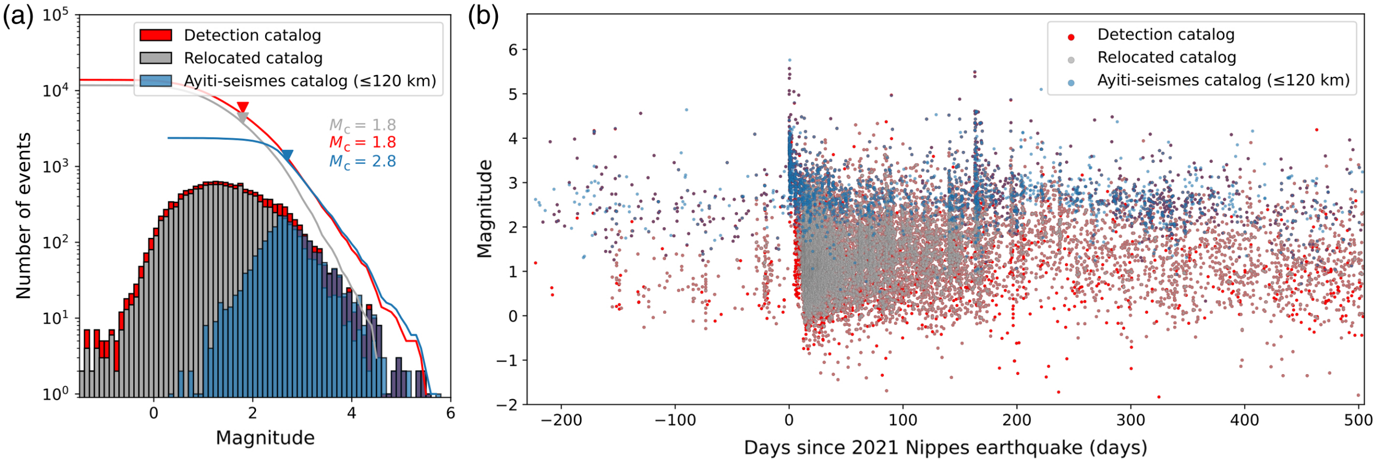

Figure 7. Magnitude distributions for the new relocated catalog (gray), detection catalog (red), and Ayiti-seismes catalog (blue). (a) Magnitude–frequency distribution, with lines showing the cumulative distribution, and triangles indicate the estimated magnitude of completeness using the maximum curvature method with a 0.2 correction (Woessner and Wiemer, 2005). (b) Magnitude distribution with time. The color version of this figure is available only in the electronic edition.

situations. Template matching shows a clear improvement applying DeepDenoiser and band-pass filtering (Fig. 4c), yielding more real detections and fewer false ones. This occurs because DeepDenoiser removes incoherent background noise more effectively than filtering alone, which also improves the MAD detection statistics, whereas the subsequent band-pass filter focuses the correlation on the dominant event frequency bands, further increasing template–signal similarity. However, despite the existence of near-real-time template matching systems (Chamberlain *et al.*, 2020), the method's computational cost and reliance on existing templates make it better suited for detailed retrospective analyses.

We therefore advise caution when deploying DeepDenoiser directly in automated earthquake monitoring. In its current form, it is unsuitable for the Ayiti-seismes workflow, but improvements are possible: augment the training set with additional RS recordings that have different coupling and noise levels, incorporate intervals containing artifacts identified by both STA/LTA and PhaseNet into the noise samples, and explore physics-based denoising methods that enforce real-world constraints (Banerjee *et al.*, 2024).

Detailed picture of the 2021 mainshock area

The majority of the events—about 67%, or 7948 earthquakes—in our new high-resolution catalog lie in the area of the 2021 M_w 7.2 Nippes earthquake (Figs. 5 and 6). In this region, we find 4.8 times more events than in the Ayiti-seismes system catalog (7948 versus 1662 on the same time interval) and 2.7 times more events than in the catalog of Douilly *et al.* (2022) (6422 versus 2417 from 20 August to 30 December 2021). The additional detections and improved locations provide a more detailed picture of the 2021 sequence and the involved fault segments (Fig. 8).

The 2021 M_w 7.2 Nippes earthquake ruptured near the Enriquillo–Plantain Garden fault (EPGF) (Calais *et al.*, 2020), an east–west left-lateral strike-slip fault that spans Haiti's southern Peninsula and extends offshore toward Jamaica (Mann *et al.*, 1995). Inversions of seismic and geodetic data show that the mainshock rupture initiated on a mostly reverse-fault segment and propagated westward to a mostly strike-slip segment (Calais *et al.*, 2022). Raimbault *et al.* (2023) identified two distinct segments: a first one dipping 66° N and mostly reverse, and a second one farther west-dipping 86° N and mostly strike-slip, associated with the Ravine du Sud fault (RSF). Douilly *et al.* (2022) also identified a multiple-segment structure, with a western segment connected to the RSF and two eastern segments dipping 60° and 70° N. They noted a near-vertical aftershock cluster near the expected EGPF extent at depth, interpreted as triggered seismicity on the EPGF, which they suggested did not rupture coseismically. Paul *et al.* (2026) expanded the aftershock catalog of Douilly *et al.* (2022) and applied the NLL-SSST-Coherence location method (Lomax and Savvaidis, 2022), identifying two clusters: a narrow western cluster parallel to the EPGF, steeply dipping northward and interpreted as the EPGF at depth; and a broader ~N110-trending cluster dipping ~70° N, interpreted as a separate reverse fault, termed the "Nippes fault."

As in Douilly *et al.* (2022) and Paul *et al.* (2026) catalogs, the aftershock distribution found here also delineates two clusters with different orientations. We analyze the aftershock distribution by examining the dip variations of the seismic clusters shown in Figure 8. Events in the western part (segments A–A′, B–B′, and C–C′ in Fig. 8) generally show a near-vertical distribution, albeit discontinuous, with a clearer lineament in segment C–C′. Between 73.81° W and 73.63° W (segment D–D′, Fig. 8e) the aftershock distribution becomes more complex, showing events still associated with the C–C′ near-vertical lineament,

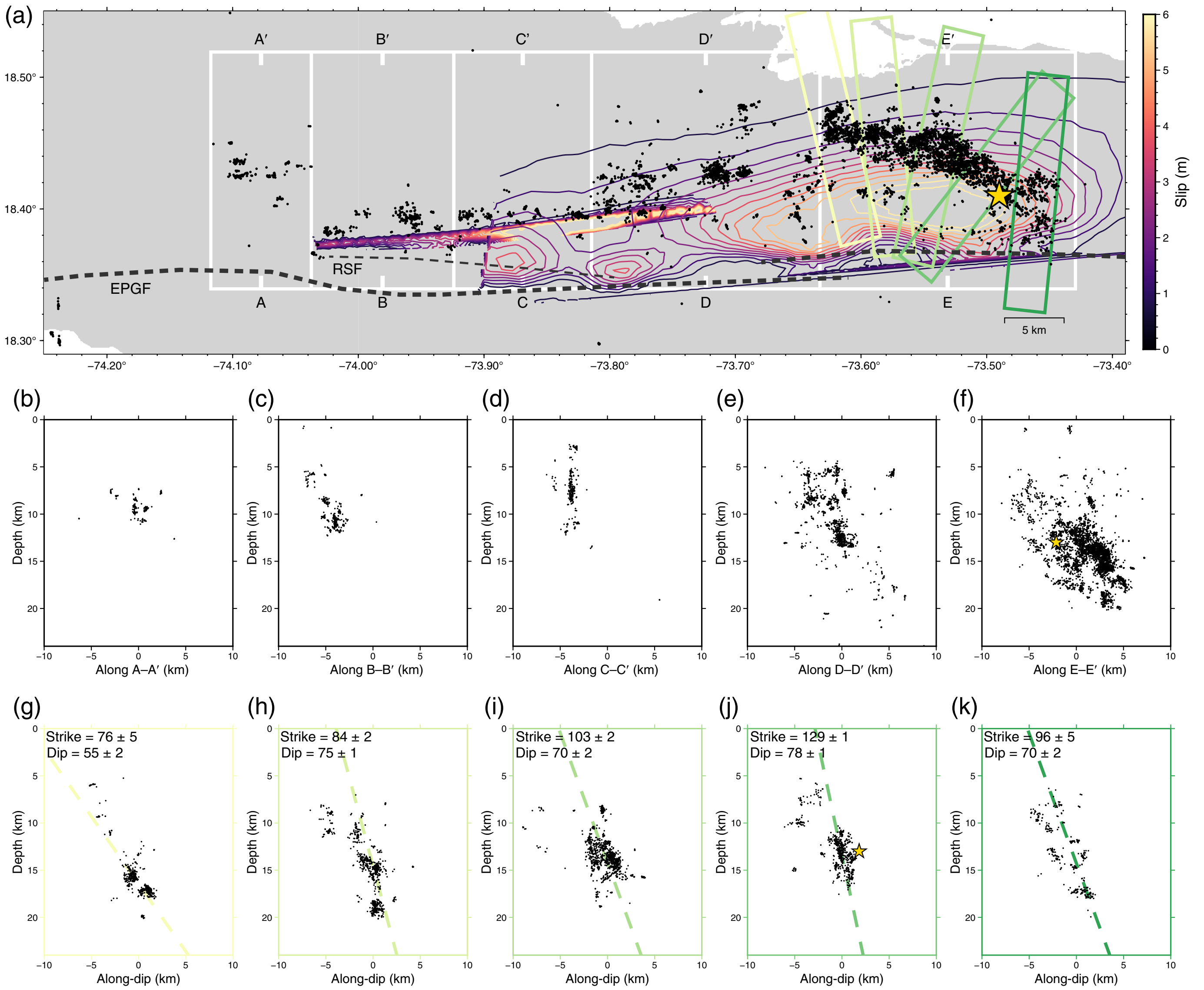

Figure 8. Spatial distribution of seismicity in our new catalog for the 2021 M_w 7.2 Nippes earthquake region. The yellow star marks the mainshock location. (a) Seismicity with coseismic rupture slip contours from Raimbault *et al.* (2023) (color denotes slip amplitude in meters). The black dashed lines show faults with surface expression from Calais *et al.* (2023). EPGF, Enriquillo–Plantain Garden fault; RSF, Ravine du Sud fault. (b–f) Cross sections along A–A′ to E–E′ profiles. (g–k) Along-dip cross sections of events within the colored rectangles in (a). Colored dashed lines show fitted fault-plane dips. The color version of this figure is available only in the electronic edition.

and additional events north of it also showing near-vertical trends. Toward the center of segment D–D′, a north-dipping cluster appears below 10 km, with a small gap to the west. West of 73.63° W, a large and complex cluster coincides with the mainshock hypocenter and most aftershocks (segment E–E′). We model this cluster by dividing it into several fault planes with equal longitudinal extent. Testing partitions from 1 to 10 planes, we select the configuration with the lowest sum of squares of differences between the observed aftershock locations and the modeled planes (Table S2). The cluster is best explained by five planes (shown in shades of green in Fig. 8a and respective cross sections in Fig. 8g–k). Consistent with (Douilly *et al.*, 2022) and Paul *et al.* (2026), this structure strikes west-southwest—east-northeast in the west, gradually rotating to an almost north-west–southeast strike to the west, up until 73.48° W, where it returns to an almost east–west strike. This structure retains a northward dip of 55° to 78° throughout its length.

The aftershock distribution aligns well with the rupture geometry and coseismic slip distribution inferred from geodetic data by Raimbault *et al.* (2023), shown with colored contours in Figure 8. The main cluster bends around the peak slip of their 66° north-dipping structure (Fig. 8a), in line with our aftershock distribution dip estimates. To the west, aftershocks in segments B–B′, C–C′, and D–D′ agree with the 86° north-dipping strike-slip segment of Raimbault *et al.* (2023), particularly in segment C–C′, which shows a similar

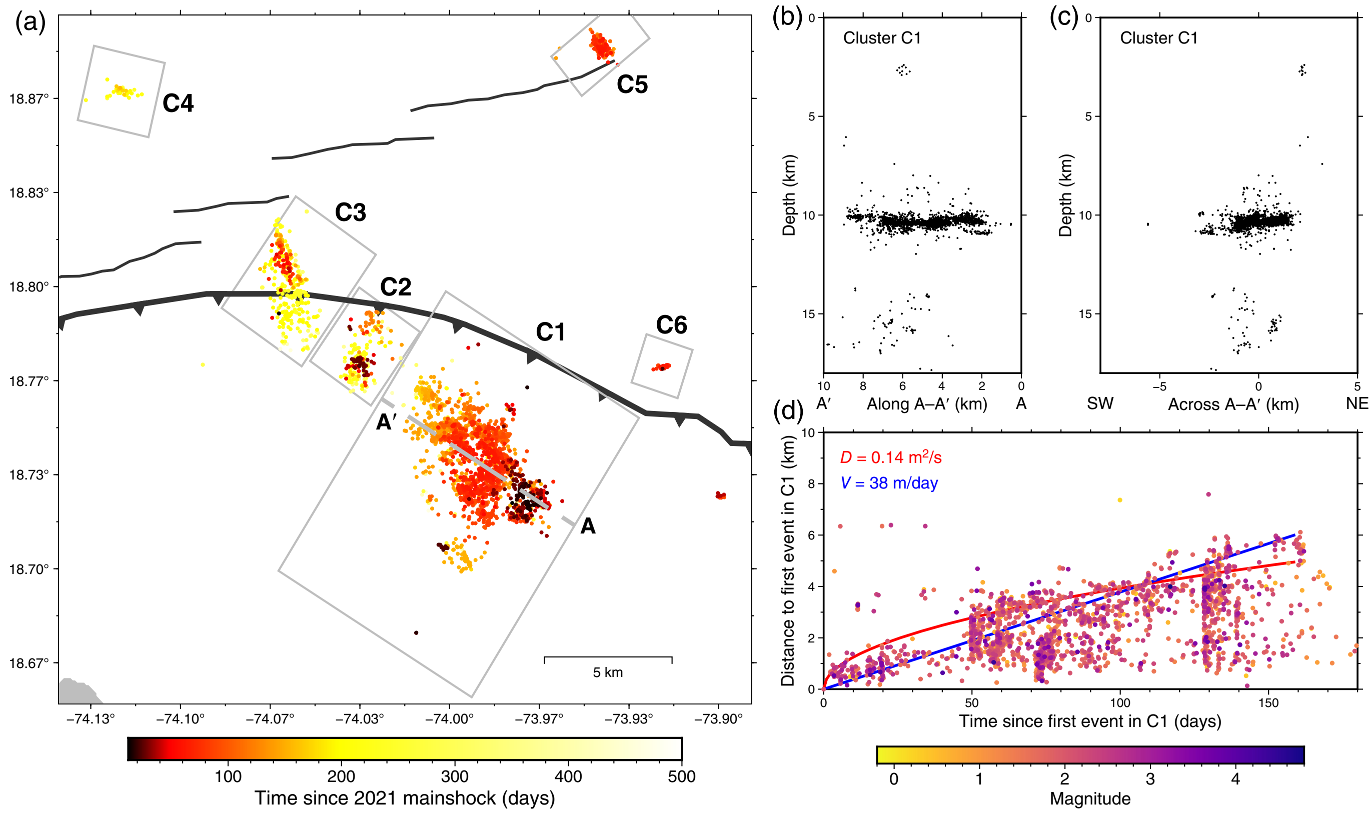

Figure 9. Jérémie basin clusters. (a) Events in the new catalog colored by occurrence time and faults from Calais *et al.* (2023). (b) Cross section of cluster C1 along A–A′. (c) Cross-section across A–A′. (d) Distance of events to the first event in C1 versus time. The blue and red lines show the best fit using linear migration and fluid diffusion models, respectively, and events are colored according to their magnitude. The color version of this figure is available only in the electronic edition.

near-vertical dip. The observed gap in segment D–D′ coincides with the meeting point of the strike-slip and reverse rupture segments found by Raimbault *et al.* (2023).

A significant difference between our catalog and that of Douilly *et al.* (2022) pertains to the distribution of aftershocks in segment E–E′ closer to the surface trace of the EGPF. This previous catalog shows a near-vertical cluster at 5–10 km depths close to the expected fault location. In our catalog, events at this location dip northward and align well with the previous modeled planes. This suggests these events are part of the reverse fault where the mainshock initiated. We find no evidence of aftershocks associated with a vertically dipping EPGF in this area.

Fluid-induced seismic swarms in the Jérémie basin?

Our new catalog reveals several offshore earthquake clusters in the Jérémie basin, NW of the 2021 mainshock epicenter (Fig. 9), also present in the Ayiti-séismes catalog (Fig. 5) but with a more spread-out distribution. Here, we identify six clusters (C1–C6) shown in Figure 9a. Cluster C1, the earliest and largest (2136 events), and clusters C2 (216 events) and C3 (358 events) are located near shallow reverse faults in the Jérémie–Malpasse fault system (Calais *et al.*, 2023). Clusters C1 and C3 delineate very low-angle SW-dipping structures consistent with identified thrust faults. Cluster C2 shows two groups of seismicity at depths of about 11 and 15 km, without clear trends (Fig. S7). In contrast, cluster C3 shows two lineaments at similar depths, but with clear SW-dipping trends (Fig. S8). Cluster C4 (48 events) is a shallow group of events at less than 3 km depth that extends in the E–W direction and shows a south-southeast (SSE) dipping (Fig. S9). Clusters C5 (123 events) and C6 (38 events) do not define clear lineaments, with C5 located above 2 km depth and C6 concentrating around 11 km depth.

These clusters exhibit swarm-like characteristics, forming spatially and temporally concentrated sequences without a clear mainshock (Mogi, 1963) (Fig. S6). For example, the largest earthquake in cluster C1 is an M 4.8 event occurring 128 days after the onset. Cluster C1 also shows a clear NW migration pattern. The other clusters also show a migrating pattern in a distance–time domain, even if their low number of events makes it less clear. Earthquake swarms are usually explained as resulting from fluid pressure diffusion (e.g., Shapiro *et al.*, 1997), aseismic slip (e.g., Roland and McGuire, 2009), or an interplay of both (e.g., Hainzl, 2004; De Barros *et al.*, 2020). We quantify the migration by defining a propagation front, adapting the methodology of previous studies (Amezawa *et al.*, 2021; Danré *et al.*, 2022).

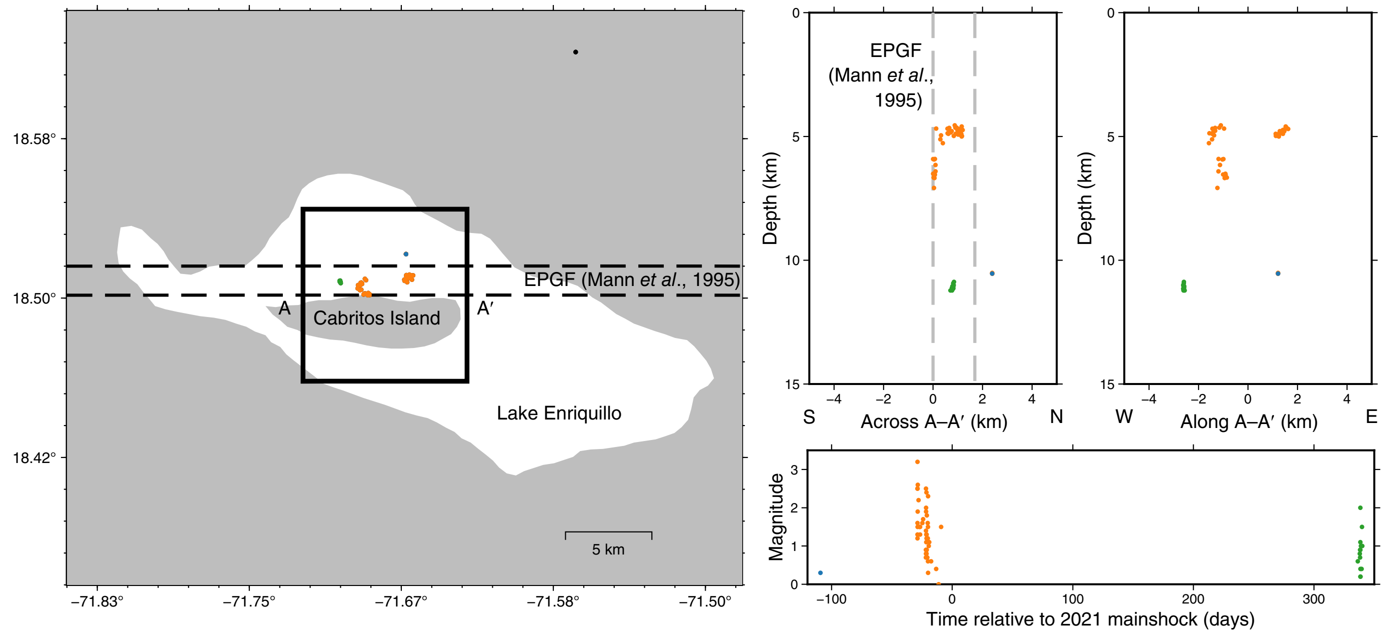

Figure 10. Seismicity in the Lake Enriquillo area. (a) Events in the new catalog, colored by temporal groups; the black-dashed lines trace the EPGF continuation proposed by Mann *et al.* (1995). (b) North–south cross section of the seismicity with the proposed EPGF continuation shown in gray. (c) West–east cross–section. (d) Magnitude distribution with time. The color version of this figure is available only in the electronic edition.

Considering the evolution of event distance to the initial event of each cluster, we define the front as the 90th percentile of the distance in nonoverlapping bins of 25 events for clusters with more than 100 events, and 10 events for smaller clusters. We fit a fluid diffusion model described by $R = \sqrt{4\pi Dt}$, in which R is the distance to the origin of the pressure source, D is the diffusivity, and t is time (Shapiro *et al.*, 1997).

Cluster C1 shows a migration pattern that can be well explained by a fluid-diffusion model (Fig. 9d). Fits on the other clusters (Figs. S8d,e and S9d) are however less clear, mainly because of the low number of events. Inferred diffusivities of 0.02–0.14 m^2/s fall into the range observed in other fluid-driven swarms (Talwani *et al.*, 2007; Chen *et al.*, 2012). The average low migration velocities between 8 and 38m/day (linear fits in Fig. 9d, Figs. S8d,e and S9d) are also consistent with fluid driven processes, while much higher velocity (>1 km/day) are expected for slow-slip driven swarms (Lohman and McGuire, 2007). This estimated migration velocity and swarm duration, for example $38\ \text{m/day} \sim 4 \times 10^{-4}\ \text{m/s}$ and about $160\ \text{days} \sim 1.4 \times 10^{7}\ \text{s}$ for cluster C1, fall in the middle of the scaling law empirically derived by Danré *et al.* (2024) for fluid-induced swarms. Therefore, both the migration pattern and velocity suggest that the swarms are driven by fluid processes, at least for swarm C1.

Evidence for seismic activity in Lake Enriquillo

The extension of the EPGF is well-documented in southern Haiti until about 72.27° W (Symithe and Calais, 2016). Further east, its extension is still debated. Mann *et al.* (1995) proposed that the EPGF continues eastward through the Enriquillo-Cul-de-Sac Valley into Lake Enriquillo, Dominican Republic, based on en échelon faults and folds (Fig. 10). Lake Enriquillo is bounded by active thrust faults (Mann *et al.*, 1995) where moderate seismic activity has been recorded (Rodriguez *et al.*, 2018; Possee *et al.*, 2019; Lee and Douilly, 2022; Escuder-Viruete *et al.*, 2025). Mann *et al.* (1995) proposed that the EPGF extends continuously to the east along the northern edge of Cabritos Island in Lake Enriquillo based on a subvertical zone of incoherent reflections on a seismic profile, though reflectors at depth on this profile are continuous across and not affected by faulting. Wang *et al.* (2018) analyzed high-resolution sonar data and proposed a continuous extension of the EPGF until at least Cabritos Island with evidence for recent activity, though again the data do not document faulting at depth. In contrast with this proposal of a continuous extent of the EPGF throughout the Cul-de-Sac–Enriquillo basin, Symithe and Calais (2016) posit that the EPGF stops around about 72.27° W and abuts against a series of reverse faults and fold–propagation folds that extend along the southern edge of the basin. This interpretation is shared by other authors on the basis of field observations (Saint Fleur *et al.*, 2019; Wessels *et al.*, 2019; Escuder-Viruete *et al.*, 2025) and of earthquake distribution (Rodriguez *et al.*, 2018; Possee *et al.*, 2019) in southern Haiti and the Dominican Republic.

Our new catalog does not resolve the eastern extent of the EPGF, but documents seismic activity near Cabritos Island (Fig. 10). We identify 62 earthquakes along the island's northern edge, where Mann *et al.* (1995) proposed the

EPGF continuation. The events occur mostly in two distinct bursts, with a group of 47 events from 21 July to 5 August 2021, the largest one of M 3.2, then a group of 14 events from 16 to 20 July 2022, the largest one of M 2.0. The seismicity extends from 4 to 11 km depth but does not align on a single, throughgoing, vertical structure. Part of the larger cluster (orange in Fig. 10a) appears near vertical, but most of it actually follows a quasi-horizontal plane just above 5 km depth. The magnitudes of the recorded earthquakes and the limited azimuthal station coverage preclude us from determining focal mechanisms that would shed light on the fault kinematics associated with the observed seismicity.

Conclusions

We explored the applicability of a deep learning denoising tool, DeepDenoiser, for seismic monitoring in Haiti. We found it is more suitable for retrospective, detailed seismicity studies than for real-time applications. When combined with template matching, DeepDenoiser enhances detection rates while reducing false positives. Doing so, we enhanced the description of Haiti's earthquake activity, tripling the number of events compared with existing catalogs. The catalog we obtained provides a detailed view of the 2021 M_w 7.2 Nippes earthquake, with aftershock distribution agreeing with recent coseismic slip models (Raimbault *et al.*, 2023) and no evidence of aftershocks associated with a vertical EPGF. It also reveals offshore swarms in the Jérémie basin with migration patterns suggesting fluid-driven processes and a distinct group of events in Lake Enriquillo, Dominican Republic, coinciding with a proposed EPGF continuation. These results show that denoising can enhance catalog completeness and quality, revealing previously unidentified areas of active seismic activity in Hispaniola.

Data and Resources

The detection and relocated catalogs are included as supplementary files (Supplemental Datasets S1 and S2). The Ayiti-seismes earthquake catalog and data from the HY network (doi: 10.7914/sn/hy) are available at the Ayiti-seismes platform (https://ayiti.unice.fr/ayiti-seismes). Data from networks AY, CN (Natural Resources Canada, 1975), CU (Albuquerque Seismological Laboratory [ASL]/U.S. Geological Survey [USGS], 2006), DR (National Seismological Centre, 1998), LO (Instituto Politecnico Loyola, 2012) can be accessed through Incorporated Research Institutions for Seismology (IRIS) web services (https://service.iris.edu/). Z2 network data will be available through IRIS web services in October 2026. Both websites were last accessed in June 2026. The supplemental material for this article includes additional information and figures on the relocated catalog, the Ayiti-seismes catalog, and the magnitude estimation procedure, together with a table summarizing the seismic stations used.

Declaration of Competing Interests

The authors acknowledge that there are no conflicts of interest recorded.

Acknowledgments

The authors acknowledge funding from the FEDER program through the Interreg Caraïbes "PREST" project (Grant 5236), the French National Research Agency "OSMOSE" (ANR-21CE03-0010) and "CAST" (ANR-22-CE01-0019) projects, and support from the Joint International Laboratory "Caribact". Quentin Bletery acknowledges funding from the European Research Council (ERC) under the European Union's Horizon 2020 research and innovation program (Grant Agreements 949221) and from the ANR—FRANCE (French National Research Agency) 3IA Cluster (Grant Agreement ANR-23-IACL-0001). Steeve J. Symithe acknowledges support from Grant and Cooperative Agreement G20AC00100 between the U.S. Geological Survey and the Faculté des Sciences of the State University of Haiti, funded by the USAID Bureau of Humanitarian Assistance, and support from the Fonds d'Appui à la Recherche of the Rectorat of the State University of Haiti. The authors thank Roby Douilly for providing access to the Z2 network. The authors thank the Associate Editor and two anonymous reviewers for their constructive comments, which improved the article.

References

Albuquerque Seismological Laboratory (ASL)/U.S. Geological Survey (USGS) (2006). Caribbean network, doi: 10.7914/SN/CU.

Allen, R. (1982). Automatic phase pickers: Their present use and future prospects, *Bull. Seismol. Soc. Am.* **72,** S225–S242.

Allen, R. V. (1978). Automatic earthquake recognition and timing from single traces, *Bull. Seismol. Soc. Am.* **68,** no. 5, 1521–1532.

Amezawa, Y., T. Maeda, and M. Kosuga (2021). Migration diffusivity as a controlling factor in the duration of earthquake swarms, *Earth Planets Space* **73,** no. 1, doi: 10.1186/s40623-021-01480-7.

Bachura, M., and T. Fischer (2019). Waveform cross-correlation for differential time measurement: Bias and limitations, *Seismol. Res. Lett.* **90,** no. 5, 2005–2014.

Bakun, W. H., C. H. Flores, and U. S. ten Brink (2012). Significant earthquakes on the enriquillo fault system, Hispaniola, 1500–2010: Implications for seismic hazard, *Bull. Seismol. Soc. Am.* **102,** no. 1, 18–30.

Banerjee, C., K. Nguyen, C. Fookes, and K. George (2024). Physics-informed computer vision: A review and perspectives, *ACM Comput. Surv.* **57,** no. 1, 17:1–17:38.

Beaucé, E., W. B. Frank, and A. Romanenko (2017). Fast matched filter (FMF): An efficient seismic matched-filter search for both CPU and GPU architectures, *Seismol. Res. Lett.* **89,** no. 1, 165–172.

Beyreuther, M., R. Barsch, L. Krischer, T. Megies, Y. Behr, and J. Wassermann (2010). Obspy: A python toolbox for seismology, *Seismol. Res. Lett.* **81,** no. 3, 530–533.

Calais, E., D. Boisson, S. Symithe, C. Prépetit, B. Pierre, S. Ulyse, L. Hurbon, A. Gilles, J.-M. Théodat, T. Monfret, *et al.* (2020). A socio-seismology experiment in Haiti, *Front. Earth Sci.* **8,** 542654.

Calais, E., A. Freed, G. Mattioli, F. Amelung, S. Jónsson, P. Jansma, S.-H. Hong, T. Dixon, C. Prépetit, and R. Momplaisir (2010). Transpressional rupture of an unmapped fault during the 2010 Haiti earthquake, *Nature Geosci.* **3,** no. 11, 794–799.

Calais, E., S. Symithe, B. M. de Lepinay, and C. Prepetit (2016). Plate boundary segmentation in the northeastern Caribbean from geodetic measurements and Neogene geological observations, *C. R. Géosci.* **348,** no. 1, 42–51.

Calais, E., S. Symithe, T. Monfret, B. Delouis, A. Lomax, F. Courboulex, J. P. Ampuero, P. E. Lara, Q. Bletery, J. Chèze, *et al.* (2022). Citizen seismology helps decipher the 2021 Haiti earthquake, *Science* **376,** no. 6590, 283–287.

Calais, E., S. J. Symithe, and B. M. de Lépinay (2023). Strain partitioning within the Caribbean–North America transform plate boundary in southern Haiti, tectonic and hazard implications, *Bull. Seismol. Soc. Am.* **113,** no. 1, 131–142.

Chamberlain, C. J., J. Townend, and M. C. Gerstenberger (2020). RT-EQcorrscan: Near-real-time matched-filtering for rapid development of dense earthquake catalogs, *Seismol. Res. Lett.* **91,** no. 6, 3574–3584.

Chen, X., P. M. Shearer, and R. E. Abercrombie (2012). Spatial migration of earthquakes within seismic clusters in Southern California: Evidence for fluid diffusion, *J. Geophys. Res. Solid Earth* **117,** no. B4, doi: 10.1029/2011JB008973.

Corbet, A., J. Célestin, L. Fallou, N. Calixte, S. Steeve, and E. Calais (2024). Qu'est-ce que faire de la science citoyenne dans un pays sans citoyens? *Etudes Caribeennes* **59,** doi: 10.4000/132zc.

Dahmen, N. L., J. F. Clinton, M.-A. Meier, S. C. Stähler, S. Ceylan, D. Kim, A. E. Stott, and D. Giardini (2022). MarsQuakeNet: A more complete marsquake catalog obtained by deep learning techniques, *J. Geophys. Res. Planets* **127,** no. 11, e2022JE007503, doi: 10.1029/2022JE007503.

Danré, P., L. De Barros, F. Cappa, and J.-P. Ampuero (2022). Prevalence of aseismic Slip linking fluid injection to natural and anthropogenic seismic swarms, *J. Geophys. Res. Solid Earth* **127,** no. 12, e2022JB025571, doi: 10.1029/2022JB025571.

Danré, P., L. De Barros, F. Cappa, and L. Passarelli (2024). Parallel dynamics of slow slips and fluid-induced seismic swarms, *Nat. Commun.* **15,** no. 1, 8943.

De Barros, L., F. Cappa, A. Deschamps, and P. Dublanchet (2020). Imbricated aseismic slip and fluid diffusion drive a seismic swarm in the Corinth Gulf, Greece, *Geophys. Res. Lett.* **47,** no. 9, e2020GL087142, doi: 10.1029/2020GL087142.

Douilly, R., S. Paul, T. Monfret, A. Deschamps, D. Ambrois, S. J. Symithe, S. St Fleur, F. Courboulex, E. Calais, D. Boisson, *et al.* (2022). Rupture segmentation of the 14 August 2021 M_w 7.2 nippes, Haiti, earthquake using aftershock relocation from a local seismic deployment, *Bull. Seismol. Soc. Am.* **113,** no. 1, 58–72.

Duverger, C., G. Mazet-Roux, L. Bollinger, A. Guilhem Trilla, A. Vallage, B. Hernandez, and Y. Cansi (2021). A decade of seismicity in metropolitan France (2010–2019): The CEA/LDG methodologies and observations, *Bull. Soc. Géol. Fr.* **192,** no. 1, 25.

Escuder-Viruete, J., F. J. Fernández, F. P. Valera, A. Medialdea, and M. Castillo-Carrión (2025). Present-day shortening accommodated by folding, thrusting and strike-slip faulting in the Enriquillo basin of southern central Hispaniola: Implications for the regional seismic hazard, *Tectonics* **44,** no. 1, e2024TC008376, doi: 10.1029/2024TC008376.

Gibbons, S. J., and F. Ringdal (2006). The detection of low magnitude seismic events using array-based waveform correlation, *Geophys. J. Int.* **165,** 149–166.

González, A. (2017). The Spanish national earthquake catalogue: evolution, precision and completeness, *J. Seismol.* **21,** no. 3, 435–471.

Hainzl, S. (2004). Seismicity patterns of earthquake swarms due to fluid intrusion and stress triggering, *Geophys. J. Int.* **159,** no. 3, 1090–1096.

Helmholtz-Centre Potsdam - GFZ German Research Centre for Geosciences and gempa GmbH (2008). The SeisComP seismological software package, *GFZ Data Services*, doi: 10.5880/GFZ.2.4.2020.003.

Hourcade, C., K. Juhel, and Q. Bletery (2025). Pegsgraph: A graph neural network for fast earthquake characterization based on prompt elastogravity signals, *J. Geophys. Res. Mach. Learn. Comput.* **2,** no. 1, e2024JH000360, doi: 10.1029/2024JH000360.

Instituto Politecnico Loyola (2012). Observatorio Sismológico Politécnico Loyola, doi: 10.7914/SN/LO.

Kagan, Y. Y. (2004). Short-term properties of earthquake catalogs and models of earthquake source, *Bull. Seismol. Soc. Am.* **94,** no. 4, 1207–1228.

Lee, H., and R. Douilly (2022). Earthquake swarms in Southern Hispaniola revealed by spatiotemporal evolution of seismicity from multi-station template matching, *Bull. Seismol. Soc. Am.* **113,** no. 1, 115–130.

Licciardi, A., Q. Bletery, B. Rouet-Leduc, J.-P. Ampuero, and K. Juhel (2022). Instantaneous tracking of earthquake growth with elastogravity signals, *Nature* **606,** no. 7913, 319–324.

Liu, M., M. Zhang, W. Zhu, W. L. Ellsworth, and H. Li (2020). Rapid characterization of the July 2019 Ridgecrest, California, earthquake sequence from raw seismic data using machine-learning phase picker, *Geophys. Res. Lett.* **47,** no. 4, e2019GL086189, doi: 10.1029/2019GL086189.

Lohman, R. B., and J. J. McGuire (2007). Earthquake swarms driven by aseismic creep in the Salton trough, California, *J. Geophys. Res. Solid Earth* **112,** no. B4, doi: 10.1029/2006JB004596.

Lomax, A., and A. Savvaidis (2022). High-precision earthquake location using source-specific station terms and inter-event waveform similarity, *J. Geophys. Res. Solid Earth* **127,** no. 1, e2021JB023190, doi: 10.1029/2021JB023190.

Mann, P., F. W. Taylor, R. L. Edwards, and T.-L. Ku (1995). Actively evolving microplate formation by oblique collision and sideways motion along strike-slip faults: An example from the northeastern Caribbean plate margin, *Tectonophysics* **246,** no. 1, 1–69.

Mogi, K. (1963). Some discussions on aftershocks, foreshocks and earthquake swarms-the fracture of a semi finite body caused by an inner stress origin and its relation to the earthquake phenomena, *Bull. Earthq. Res. Inst.* **41,** 615–658.

Mousavi, S. M., W. L. Ellsworth, W. Zhu, L. Y. Chuang, and G. C. Beroza (2020). Earthquake transformer—An attentive deep-learning model for simultaneous earthquake detection and phase picking, *Nat. Commun.* **11,** no. 1, 3952.

Münchmeyer, J., D. Bindi, U. Leser, and F. Tilmann (2021). Earthquake magnitude and location estimation from real time seismic waveforms with a transformer network, *Geophys. J. Int.* **226,** no. 2, 1086–1104.

National Seismological Centre (1998). Centro Nacional de Sismologia, doi: 10.7914/SN/DR.

Natural Resources Canada (1975). Canadian national seismograph network, doi: 10.7914/SN/CN.

Neves, M., Z. Peng, and G. Lin (2022). A high-resolution earthquake catalog for the 2004 M_w 6 Parkfield earthquake sequence using a matched filter technique, *Seismol. Res. Lett.* **94,** no. 1, 507–521.

Paul, S., T. Monfret, E. Calais, F. Courboulex, B. Delouis, A. Lomax, B. M. de Lépinay, S. J. Symithe, A. Deschamps, D. Ambrois, *et al.*

(2026). Precise relocation of the 14 august 2021 mw 7.2 nippes, Haiti, earthquake sequence using broadband and citizen-hosted short-period seismometers, *Tectonophysics* **918,** 230982.

Paul, S., T. Monfret, F. Courboulex, J. Chèze, E. Calais, S. Julien Symithe, A. Deschamps, F. Peix, D. Ambrois, X. Martin, *et al.* (2023). Monitoring of local earthquakes in Haiti using low-cost, citizen-hosted seismometers and regional broadband stations, *Seismol. Res. Lett.* **94,** no. 6, 2725–2739.

Peng, Z., J. E. Vidale, and H. Houston (2006). Anomalous early aftershock decay rate of the 2004 M_w 6.0 Parkfield, California, earthquake, *Geophys. Res. Lett.* **33,** no. 17, doi: 10.1029/2006GL026744.

Possee, D., D. Keir, N. Harmon, C. Rychert, F. Rolandone, S. Leroy, J. Corbeau, G. Stuart, E. Calais, F. Illsley-Kemp, *et al.* (2019). The tectonics and active faulting of Haiti from seismicity and tomography, *Tectonics* **38,** no. 3, 1138–1155.

Raimbault, B., R. Jolivet, E. Calais, S. Symithe, Y. Fukushima, and P. Dubernet (2023). Rupture geometry and slip distribution of the M_w 7.2 Nippes earthquake, Haiti, from space geodetic data, *Geochem. Geophys. Geosys.* **24,** no. 4, e2022GC010752, doi: 10.1029/2022GC010752.

Rodriguez, J., J. Havskov, M. B. Sørensen, and L. F. Santos (2018). Seismotectonics of south-west Dominican Republic using recent data, *J. Seismol.* **22,** no. 4, 883–896.

Roland, E., and J. J. McGuire (2009). Earthquake swarms on transform faults, *Geophys. J. Int.* **178,** no. 3, 1677–1690.

Ross, Z. E., M.-A. Meier, E. Hauksson, and T. H. Heaton (2018). Generalized seismic phase detection with deep learning, *Bull. Seismol. Soc. Am.* **108,** no. 5A, 2894–2901.

Saint Fleur, N., N. Feuillet, and Y. Klinger (2019). Active tectonics along the Cul-de-Sac–Enriquillo plain and seismic hazard for Port-au-Prince, Haiti, *Tectonophysics* **771,** 228235.

Shapiro, S. A., E. Huenges, and G. Borm (1997). Estimating the crust permeability from fluid-injection-induced seismic emission at the KTB site, *Geophys. J. Int.* **131,** no. 2, F15–F18.

Styron, R., J. García-Pelaez, and M. Pagani (2020). Ccaf-db: The Caribbean and central American active fault database, *Nat. Hazards Earth Syst. Sci.* **20,** no. 3, 831–857.

Symithe, S., and E. Calais (2016). Present-day shortening in southern haiti from gps measurements and implications for seismic hazard, *Tectonophysics* **679,** 117–124.

Talwani, P., L. Chen, and K. Gahalaut (2007). Seismogenic permeability, ks, *J. Geophys. Res. Solid Earth* **112,** no. B7, doi: 10.1029/2006JB004665.

Tan, Y. J., F. Waldhauser, W. L. Ellsworth, M. Zhang, W. Zhu, M. Michele, L. Chiaraluce, G. C. Beroza, and M. Segou (2021). Machine-learning-based high-resolution earthquake catalog reveals how complex fault structures were activated during the 2016–2017 central italy sequence, *The Seism. Rec.* **1,** no. 1, 11–19.

van den Ende, M. P., and J.-P. Ampuero (2020). Automated seismic source characterization using deep graph neural networks, *Geophys. Res. Lett.* **47,** no. 17, e2020GL088690, doi: 10.1029/2020GL088690.

Waldhauser, F., and W. L. Ellsworth (2000). A double-difference earthquake location algorithm: Method and application to the northern Hayward fault, California, *Bull. Seismol. Soc. Am.* **90,** no. 6, 1353–1368.

Wang, J., P. Mann, and R. R. Stewart (2018). Late holocene structural style and seismicity of highly transpressional faults in southern Haiti, *Tectonics* **37,** no. 10, 3834–3852.

Wessels, R. J., N. Ellouz-Zimmermann, N. Bellahsen, Y. Hamon, C. Rosenberg, R. Deschamps, R. Momplaisir, D. Boisson, and S. Leroy (2019). Polyphase tectonic history of the Southern Peninsula, Haiti: From folding-and-thrusting to transpressive strike-slip, *Tectonophysics* **751,** 125–149.

Wickham-Piotrowski, A., Y. Font, M. Regnier, B. Delouis, O. Lengliné, M. Segovia, and Q. Bletery (2024). Achieving a comprehensive microseismicity catalog through a deep-learning-based workflow: Applications in the central Ecuadorian subduction zone, *Bull. Seismol. Soc. Am.* **114,** no. 2, 823–841.

Woessner, J., and S. Wiemer (2005). Assessing the quality of earthquake catalogues: Estimating the magnitude of completeness and its uncertainty, *Bull. Seismol. Soc. Am.* **95,** no. 2, 684–698.

Woollam, J., J. Münchmeyer, F. Tilmann, A. Rietbrock, D. Lange, T. Bornstein, T. Diehl, C. Giunchi, F. Haslinger, D. Jozinović, *et al.* (2022). SeisBench—A toolbox for machine learning in seismology, *Seismol. Res. Lett.* **93,** no. 3, 1695–1709.

Yang, L., X. Liu, W. Zhu, L. Zhao, and G. C. Beroza (2022). Toward improved urban earthquake monitoring through deep-learning-based noise suppression, *Sci. Adv.* **8,** no. 15, eabl3564, doi: 10.1126/sciadv.abl3564.

Zhang, M., W. L. Ellsworth, and G. C. Beroza (2019). Rapid earthquake association and location, *Seismol. Res. Lett.* **90,** no. 6, 2276–2284.

Zhu, W., and G. C. Beroza (2019). PhaseNet: A deep-neural-network-based seismic arrival-time picking method, *Geophys. J. Int.* **216,** no. 1, 261–273.

Zhu, W., S. M. Mousavi, and G. C. Beroza (2019). Seismic signal denoising and decomposition using deep neural networks, *IEEE Trans. Geosci. Remote Sens.* **57,** no. 11, 9476–9488.

Manuscript received 18 November 2025
Published online 2 July 2026